Enhancing T_1 magnetic resonance imaging contrast with internalized gadolinium(III) in a multilayer nanoparticle

Valeria S. Marangoni[a,b,1], Oara Neumann[c,d,1], Luke Henderson[a,d], Caterina C. Kaffes[e], Hui Zhang[d,f], Runmin Zhang[d,f], Sandra Bishnoi[a], Ciceron Ayala-Orozco[a], Valtencir Zucolotto[b], James A. Bankson[e], Peter Nordlander[d,f], and Naomi J. Halas[a,c,d,f,2]

[a]Department of Chemistry, Rice University, Houston, TX 77005; [b]Sao Carlos Institute of Physics, University of Sao Paulo, Sao Carlos, Sao Paulo 13566-590, Brazil; [c]Department of Electrical and Computer Engineering, Rice University, Houston, TX 77005; [d]Laboratory for Nanophotonics, Rice University, Houston, TX 77005; [e]Department of Imaging Physics, The University of Texas M. D. Anderson Cancer Center, Houston, TX 77030; and [f]Department of Physics and Astronomy, Rice University, Houston, TX 77005

Contributed by Naomi J. Halas, May 18, 2017 (sent for review February 14, 2017; reviewed by Paolo Decuzzi and Teri W. Odom)

Multifunctional nanoparticles for biomedical applications have shown extraordinary potential as contrast agents in various bioimaging modalities, near-IR photothermal therapy, and for light-triggered therapeutic release processes. Over the past several years, numerous studies have been performed to synthesize and enhance MRI contrast with nanoparticles. However, understanding the MRI enhancement mechanism in a multishell nanoparticle geometry, and controlling its properties, remains a challenge. To systematically examine MRI enhancement in a nanoparticle geometry, we have synthesized MRI-active Au nanomatryoshkas. These are Au core–silica layer–Au shell nanoparticles, where Gd(III) ions are encapsulated within the silica layer between the inner core and outer Au layer of the nanoparticle (Gd-NM). This multifunctional nanoparticle retains its strong near-IR Fano-resonant optical absorption properties essential for photothermal or other near-IR light-triggered therapy, while simultaneously providing increased T_1 contrast in MR imaging by concentrating Gd(III) within the nanoparticle. Measurements of Gd-NM revealed a strongly enhanced T_1 relaxivity ($r_1 \sim 24\ mM^{-1}{\cdot}s^{-1}$) even at 4.7 T, substantially surpassing conventional Gd(III) chelating agents ($r_1 \sim 3\ mM^{-1}{\cdot}s^{-1}$ at 4.7 T) currently in clinical use. By varying the thickness of the outer gold layer of the nanoparticle, we show that the observed relaxivities are consistent with Solomon–Bloembergen–Morgan (SBM) theory, which takes into account the longer-range interactions between the encapsulated Gd(III) and the protons of the H_2O molecules outside the nanoparticle. This nanoparticle complex and its MRI T_1-enhancing properties open the door for future studies on quantitative tracking of therapeutic nanoparticles in vivo, an essential step for optimizing light-induced, nanoparticle-based therapies.

T_1 MRI contrast | gadolinium | Au nanoparticle | relaxivity

Multicomponent nanoparticle complexes have received great attention as theranostic agents (having both diagnostic and therapeutic functions) due to the unique properties that can be combined within a single nanostructure (1–4). These include intense near-IR (NIR) optical absorption due to a strong localized surface plasmon resonance, in vivo/in vitro stability, biocompatibility, facile surface conjugation chemistry (5–8), and their use as contrast agents in magnetic resonance imaging (MRI) applications. MRI is currently the most universally used biomedical imaging modality (9). It is a noninvasive technique with contrast versatility and high spatial and temporal resolution (10, 11). There are two main types of MRI contrast agents currently in widespread clinical use (9). T_2-weighted contrast agents locally modify the spin–spin relaxation process of water protons, producing negative or dark images (based on materials such as superparamagnetic Fe_3O_4 nanoparticles) (12). T_1-weighted contrast agents affect nearby protons through spin–lattice relaxation, producing positive (bright) image contrast [based on paramagnetic materials such as Gd(III) and Mn(II)] (11, 13). The ability of a contrast agent to change the longitudinal ($1/T_1$) or transverse ($1/T_2$) relaxation rate is measured as relaxivity, r_1 or r_2, respectively, which is characterized as the change in relaxation rate after the introduction of the contrast agent normalized to the concentration of the contrast agent. Despite their utility, T_2 contrast agents also have several disadvantages that limit their use in clinical applications. They can cause a reduction in the MRI signal, which can be confused with other pathogenic conditions (such as blood clots and endogenous iron) (11). In the case of tumor imaging, they can induce magnetic field perturbations on the protons in neighboring normal tissue, which can make spatially well-resolved diagnosis difficult (11). In contrast, T_1 contrast agents increase the specificity and sensitivity of the MR image. Among the paramagnetic materials useful for T_1 contrast MR imaging, Gd(III) is the most effective contrast agent currently available for clinical use. However, free Gd(III) ions have high toxicity, and Gd(III)-chelates currently in clinical use, such as 1,4,7,10-tetraazacyclododecane-1,4,7,10-tetraacetic acid (DOTA) and diethylenetriaminepentaacetic acid (DTPA), suffer from poor sensitivity ($r_1 \sim 3\ mM^{-1}{\cdot}s^{-1}$ at 4.7 T), rapid renal clearance, and lack of specificity due to their small molecular size (10, 14). Considerable efforts have been

Significance

We demonstrate a magnetic resonance image-enhancing nanoparticle with the potential for use in multiple biomedical imaging and therapeutic applications. The nanoparticle contains internal gadolinium ions for T_1 imaging contrast, located between an inner core and outer Au layer, in a multilayered geometry. The proton relaxivity is enhanced through longer-range interactions with the protons outside the nanoparticle, a radical departure from the molecular chelates currently in use for MRI. This geometry provides a very large relaxivity enhancement ($r_1 \sim 24\ mM^{-1}{\cdot}s^{-1}$) compared with conventional chelating agents (Gd-DOTA: $r_1 \sim 3\ mM^{-1}{\cdot}s^{-1}$) at high magnetic fields (4.7 T). This MRI-enhancing nanoparticle geometry opens opportunities for the development of multifunctional MRI-active nanoparticles for biomedical applications.

Author contributions: V.S.M., O.N., V.Z., J.B., P.N., and N.J.H. designed research; V.S.M., O.N., L.H., C.K., H.Z., R.Z., S.B., and C.A.-O. performed research; H.Z., R.Z., and P.N. analyzed data; and V.S.M., O.N., V.Z., J.B., P.N., and N.J.H. wrote the paper.

Reviewers: P.D., Istituto Italiano di Tecnologia–Genova; and T.W.O., Northwestern University.

The authors declare no conflict of interest.

Freely available online through the PNAS open access option.

[1]V.S.M. and O.N. contributed equally to this work.

[2]To whom correspondence should be addressed. Email: halas@rice.edu.

This article contains supporting information online at www.pnas.org/lookup/suppl/doi:10.1073/pnas.1701944114/-/DCSupplemental.

devoted to the incorporation of Gd(III) onto or into nanoparticles that will enhance their sensitivity by increasing their specificity, prolonging circulation time, and reducing their toxicity. Furthermore, these nanostructured Gd(III) agents present enhanced relaxivity compared with free Gd(III) chelates due to both cumulative effect of the high number of Gd(III) ions per nanocarrier and the reduced global tumbling motion that enhance the r_1 of each nanocomplex (10, 15–19).

Recently, we developed tunable plasmonic Au nanomatryoshkas (NMs), a metal-based nanoparticle consisting of a Au core, an interstitial nanoscale SiO_2 layer, and an outer Au shell (20, 21). This nanoparticle possesses a strong optical extinction at 800 nm, resulting in strong local photothermal heating (21), which makes it a highly attractive candidate for NIR photothermal cancer therapy. Besides the biocompatibility and facile surface conjugation chemistry made possible by its outer Au layer (22), this system has been shown to have several advantages compared with other NIR photothermal transducers. For example, tumor uptake of NM (~90-nm diameter) in a triple-negative breast cancer model was fourfold to fivefold higher than Au nanoshells (~150-nm diameter), and consequently NM displayed an improved photothermal therapy efficacy relative to nanoshells (21).

Here, we report a modification of NMs that transforms them into high-relaxivity MRI-active contrast agents. This was accomplished by incorporating Gd(III) into the interstitial silica layer of the NM structure. The geometry of this nanoparticle as an MRI contrast agent is both surprising and counterintuitive. The T_1 enhancement mechanism of molecular contrast agents, which typically consist of a single Gd(III) ion surrounded by chelating ligands, relies upon extremely close distances between the Gd(III) ions within the molecule and nearby H_2O protons. Our layered nanoparticle strategy yields nanoparticle complexes with higher T_1 relaxivities than molecular T_1 contrast agents, but in this system, the Gd(III) ions are well-separated from the H_2O protons outside the nanoparticle. Our main goal was to evaluate the influence of structural nanoparticle parameters such as the number of Gd(III) inside the particle, Au shell thickness, and surface functionalization on the relaxivity (r_1) of the Gd-NM, and to elucidate the relaxivity mechanism. This study resulted in an optimized Gd-NM system with good T_1 relaxivity at high magnetic field strength (4.7 T) and significantly enhanced T_1 relaxivities compared with molecular contrast agents. Furthermore, an MRI T_1-weight relaxivity mechanism of Gd-NM was elucidated by systematically varying and controlling the layered nanostructure morphology.

Gd-NM nanoparticles were fabricated as shown in Fig. 1*A*. Transmission electron microscope images corresponding to each stage of the synthesis are shown (Fig. 1*Bi–iv*). The synthesis developed here is modified from one reported previously to incorporate dyes within a plasmonic structure to enhance their fluorescence (23). Au nanoparticles of diameter 50 ± 4 nm (Fig. 1*Bi*) were initially coated with a 21 ± 2-nm amorphous silica layer doped with *S*-2(4-isothiocyanatobenzyl)-1,4,7,10-tetraazacyclododecane-1,4,7,10-tetraacetic acid (SCN-DOTA) chelates (Fig. 1*Bii*). The isothiocyanate (N=C=S) group of the SCN-DOTA chelate is believed to bind covalently to the NH_2 group of the 3-aminopropyl) triethoxysilane (APTES) molecules within the silica network. This results in the formation of a thiourea [NH–(C=S)–NH] bond that was monitored by Fourier transform infrared (FTIR) measurements (Fig. S1*A* shows the FTIR spectra and the peak assignments). As a result of the formation of this bond, the peak at 2,100 cm^{-1} (attributed to the N=C=S vibration in the SCN-DOTA chelate molecules) disappears after coupling of the chelate with APTES (24), but the C=S band around 1,100 cm^{-1} can be observed, indicating the thiourea formation. The Gd(III) ions were loaded into the chelates by incubating the nanoparticles at this stage with a solution of $Gd(NO_3)_3$.

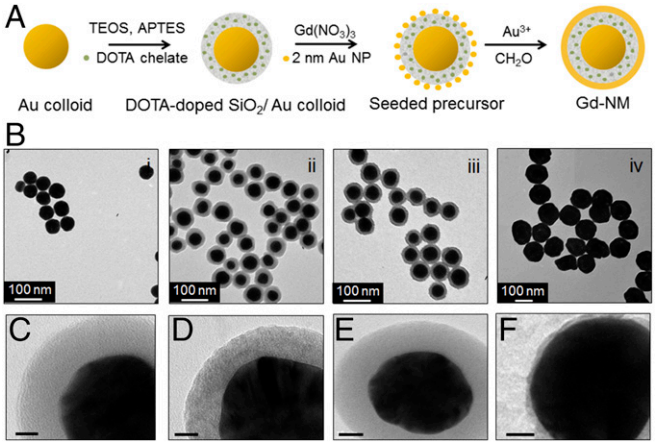

Fig. 1. (*A*) Schematic representation of the MRI-active NM synthesis showing the stepwise synthesis process: the 50-nm-diameter gold colloids are coated with SCN-DOTA chelates embedded in a SiO_2 shell, and then incubated in $Gd(NO_3)_3$ and 2-nm Au NP, followed by the growth of a continuous Au shell. (*B*) TEM images corresponding to each step in the process. (Scale bars: 100 nm.) The silica etching process during the incubation with Gd $(NO_3)_3$ step: high-resolution TEM images of SCN-DOTA chelate-doped SiO_2-coated Au colloid (*C*) before and (*D*) after incubation with $Gd(NO_3)_3$ solution, and SiO_2-coated Au colloid (*E*) before and (*F*) after incubation with Gd $(NO_3)_3$ solution. (Scale bars: 10 nm.)

The effect of the SCN-DOTA and Gd(III) loaded within the SiO_2 layer of Au@SiO_2 particles was examined by high-resolution transmission electron microscopy (TEM) shown in Fig. 1 *C–F*. The TEM images reveal that, when the chelate is embedded into the silica layer, the $Gd(NO_3)_3$ solution etches ~8 nm of the inner-silica shell (Fig. 1 *C* and *D*). However, when the chelates are not part of the silica network, the $Gd(NO_3)_3$ solution etches the silica shell almost completely (Fig. 1 *E* and *F*). The porosity of the silica shell is affected by the Stöber synthesis parameters, such as the ratio between H_2O and tetraethoxysilane (TEOS), the reaction pH, salt, and the catalysis molecules. A simple addition of APTES-SCN-DOTA (Fig. S1*B*) solution in ethanol during the silica growth process results in a different network structure with more defect sites compared with the TEOS network alone, which is more resistant to the etching process of $Gd(NO_3)_3$ (25–27). The difference in the particle's surface functionality and porosity can be examined by TEM (Fig. 1 *C–F*) and ζ-potential measurements. In the case of Au@SiO_2 nanoparticles, the ζ-potential is around −10 mV, whereas the Au@SiO_2-SCN-DOTA ζ-potential becomes neutral or slightly positive due to the lack of silanol (Si–OH) groups. As a result, the Au@SiO_2-SCN-DOTA nanoparticles are more stable in the acidic conditions compared with classical Au@SiO_2 system where the negatively charged SiO^- are dissociated from the functional Si–OH groups in the acidic conditions (28). The different observed etching of the silica layer by the $Gd(NO_3)_3$ with and without SCN-DOTA is evidence that the chelate is attached in the silica network. The Gd(III) salt also increased the stability of the particles in the following steps, such as formation of the seeded precursor and growth of the final gold shell.

After growth of the Gd(III)-embedded silica layer, 2- to 3-nm-diameter Au colloidal nanoparticles were attached to the outer surface of the silica layer. At this stage, we refer to the nanoparticles as the "seeded precursor." The ultrasmall Au nanoparticles serve as nucleation sites for the electroless plating of the outer Au shell layer (Fig. 1*Biii*). This results in Gd-NMs with average dimensions of $[r'1, r'2, r'3] = [25 \pm 3, 38 \pm 2, 53 \pm 2]$ nm (Fig. 1*Biv*), where r′1, r′2, and r′3 correspond to the radii of Au, Au@SiO_2-SCN-DOTA, and Au@SiO_2-Gd-SCN-DOTA@Au

CHEMISTRY

(Gd-NM), respectively. This multistep synthesis produces stable, monodisperse Gd-NM with a continuous outer Au layer (Fig. S2). The final Au shell also allows straightforward conjugation of polymers and biomolecules to the nanoparticle surface.

To optimize the MRI contrast of the Gd-NMs, the concentration of Gd(III) per particle was varied by modifying the chelate concentration and reaction time. The Gd(III) concentration on Gd-NM was checked after each step in the synthesis by inductively coupled plasma mass spectroscopy (ICP-MS). For the MRI measurements, the concentration of the particles from each individual synthesis was adjusted by dilution to have 5, 10, 15, and 20 μM Gd(III) ions. The MRI relaxivity as a function of Gd(III) concentration is shown in Fig. 2. The relaxivities (r_1) were calculated from the $1/T_1$ vs. Gd(III) concentration data. (Detailed information about relaxivity and the T_1 relaxivity curves for three representative concentrations are shown in Fig. S3.) We observed that, at low Gd(III) concentrations, the MRI relaxivity r_1 increased with increasing Gd(III) concentration per NM. For example, the relaxivity of 0.7×10^5 Gd(III) ions/NM was 8 $mM^{-1}{\cdot}s^{-1}$ and increased until a maximum of 14.6 $mM^{-1}{\cdot}s^{-1}$ at 2.5×10^5 Gd(III) ions/NM was reached. As the amount of Gd(III) per NM was increased further to 8.2×10^5 Gd(III)/NM, the relaxivity decreased to 5.3 $mM^{-1}{\cdot}s^{-1}$. This type of quenching effect has been observed in other nanoparticle-based Gd(III) systems developed for MRI (8, 25, 29). In these cases, quenching was attributed to the packing of Gd(III) into a limited volume, which could restrict the access of H_2O molecules to the coordination sphere of the Gd(III). However, as we will discuss shortly, our results indicate that, in the case of Gd-NMs, the inner coordination sphere H_2O molecules have a reduced effect on the enhanced T_1 relaxivity (Fig. S4 shows the effect of the accumulation of water molecules in the silica inner layer). It has additionally been proposed that systems with an excessive payload of Gd(III) may lead to a disproportionate weight of T_2 effects, which would have a negative effect on T_1-weighted images (8, 25, 27, 28). We did observe an increase in T_2 relaxivity by increasing the number of Gd(III) per nanoparticle. For example, for a system with 2.3×10^5 Gd(III) per nanoparticle, the r_2 was nominally 54.7 $mM^{-1}{\cdot}s^{-1}$, whereas for 4.7×10^5 it was 93.6 $mM^{-1}{\cdot}s^{-1}$. This increase in T_2 relaxivity has, in other nanoparticle systems, been attributed to the geometric confinement of Gd(III) with increased dipolar interaction between neighboring Gd(III)–Gd(III) ions and/or Curie spin relaxation (29).

To better understand how this specific geometry impacts the Gd-NM relaxivity, we examine how the relaxivity is modified at the various stages of nanoparticle synthesis. A comparative study of T_1 relaxivity vs. Gd(III) concentration within the internal silica layer was performed for the seeded precursor (Fig. 3*A*) and the complete Gd-NM-PEG (Fig. 3*B*). For each structure, this information is accompanied by the corresponding extinction spectrum (Fig. 3 *C* and *D*) and TEM images (Fig. 3 *E* and *F*). All measurements were performed at 4.7 T. The r_1 values were calculated to be 21.5 and 17.9 $mM^{-1}{\cdot}s^{-1}$ for the seeded precursor and Gd-NM-PEG, respectively. We find that the addition of the Au outer shell to the seeded precursor nanoparticle decreases its relaxivity, because the growth of a continuous metal shell layer limits access of water molecules to the coordination spheres of the Gd(III) within the interior silica layer. However, considering the Gd(III) per nanoparticle, the relaxivity per nanoparticle was calculated to be $\sim 2.7 \times 10^5$ $mM^{-1}{\cdot}s^{-1}$ for Gd-NM-PEG. For comparison, molecular chelate Gd(III) contrast agents in current clinical use typically have relaxivities r_1 of about 3 $mM^{-1}{\cdot}s^{-1}$ per Gd(III) at 4.7 T and 37 °C (30). As shown in the T_1-weighted MRI images (Fig. 3 *A* and *B*, Insets), the seeded precursors produced consistently brighter images than the Gd-NM-PEG. There are two primary differences between the seeded precursor and the final NM that would affect the relaxivity. First, the seeded precursor lacks an outer Au shell and would allow for greater interaction and shorter distances between the contrast agent and water protons. If this was the only difference between the two systems, we would expect the relaxivity to be considerably greater in the seeded precursor compared with the NM. However, the addition of the outer Au shell adds more mass to the particle and further reduces the molecular tumbling rate of the contrast agent, increasing the relaxivity. Furthermore, the final Gd-NM is also PEGylated, further reducing the tumbling rate. As a result of these differences, the seeded precursor has only a slightly higher relaxivity compared with the final NM.

The enhanced relaxivities of Gd(III)-containing nanostructures relative to molecular chelates can be attributed not only to the additive effect of many Gd(III) centers but also to their slower rotational motion (13, 31). According to the Solomon–Bloembergen–Morgan (SBM) theory of paramagnetic relaxation, the main factors that affect the relaxivity of Gd(III)-based contrast agents are molecular diffusional and rotational times, number of coordinated water molecules, water proton residency lifetime, and water exchange rate (32). In general, a decrease in the molecular diffusion and rotation times leads to an increased T_1 relaxivity, especially at low magnetic fields (13, 33). Therefore, the incorporation of Gd(III) into nanostructures decreases its molecular tumbling rate and, consequently, reduces its diffusional and rotational correlation time, increasing relaxivity (32). Besides the enhanced T_1 relaxivity, another important advantage of nanostructured systems is the increased accumulation of carriers in target tissue. For example, the enhanced permeability and retention effect in tumors can be exploited for passive targeting using nanoparticles (34), which increases the local concentration of the contrast agent in the tumor (32).

It is worth emphasizing that our measurements were performed at 4.7 T. Higher magnetic fields provide not only a greater signal to noise, but also a higher spatial resolution and reduced acquisition times (33). However, the T_1 relaxivity of molecular Gd(III) compounds typically decreases as the magnetic field increases (30, 33). For example, the relaxivity of Gd-NM was 24.5 $mM^{-1}{\cdot}s^{-1}$ at 4.7 T and 54.7 $mM^{-1}{\cdot}s^{-1}$ at 1 T (Fig. S5). The effect of the magnetic field on the relaxivity was shown to be more pronounced for slowly tumbling molecules than for rapidly tumbling molecules (33). Small molecules such as Gd-DTPA or MS-325 show a modest decrease in r_1 with field; however, for MS-325 bound to serum albumin, the relaxivity decreases from 24.3 $mM^{-1}{\cdot}s^{-1}$ at 1.4 T to 11.2 $mM^{-1}{\cdot}s^{-1}$ at 4.7 T. Similarly, Gd(III)-chelate–functionalized gold nanostars showed a r_1 relaxivity of 54.7 $mM^{-1}{\cdot}s^{-1}$ at 1.41 T that was reduced to 9.4 $mM^{-1}{\cdot}s^{-1}$ at 7 T (19). Therefore, it is a major challenge to develop MRI contrast agents that have a

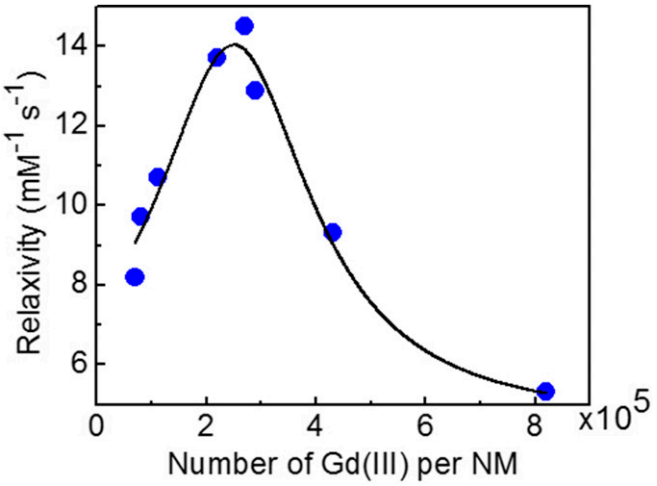

Fig. 2. The r_1 relaxivity of Gd-NM as a function of the number of Gd(III) per NM measured at 4.7 T (blue dots) and nonlinear curve fit (black line). Gd(III) concentration was quantified using ICP-MS.

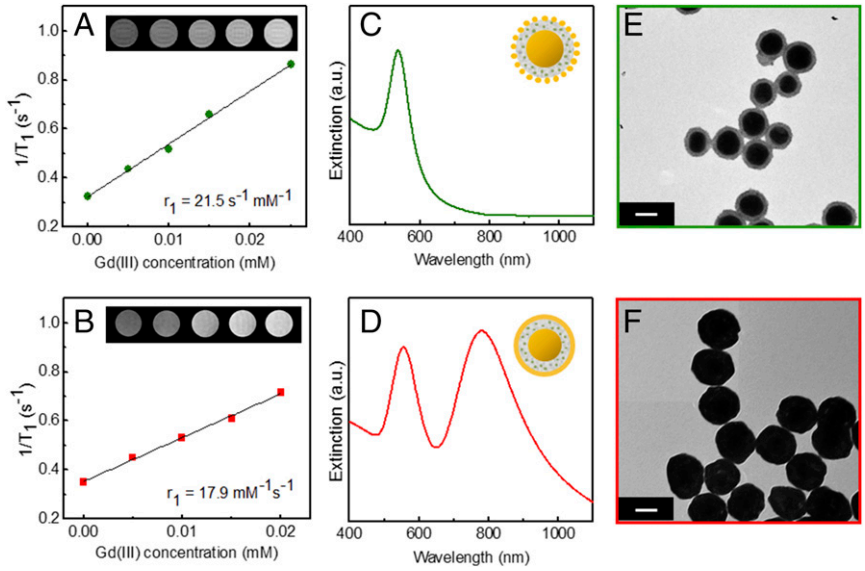

Fig. 3. T_1 (longitudinal) rate vs. Gd(III) concentration at 4.7 T for (*A*) seeded precursor, (*B*) Gd-NM-PEG, and the corresponding (*C* and *D*) extinction spectra and (*E* and *F*) TEM images. (Scale bars: 50 nm.) (*Insets A* and *B*: T_1-weighted MR images.)

high r_1 and can also be used at higher magnetic fields. Gd-NMs appear to be an attractive candidate for higher-field MRI applications.

The MRI contrast mechanism depends not only on the T_1 or T_2 relaxation rate, but also on the proton density in the surrounding medium and the distance between the proton nuclei and the Gd(III) (35). To investigate the effect of the distance between the proton nucleus and the encapsulated Gd(III) on the T_1 MRI mechanism, Gd-NM-PEG structures with four different outer Au layer thicknesses were fabricated and investigated. The T_1 longitudinal rates at 4.7 T for the Gd-NM-PEG nanoparticles with different gold outer shell thickness (radii) ([r′1, r′2, r′3] = [25, 38, 51 nm]), ([r′1, r′2, r′3] = [25, 38, 53 nm]), ([r′1, r′2, r′3] = [25, 38, 56 nm]), and the thicker shell ([r′1, r′2, r′3] = [25, 38, 73 nm]) are shown in Fig. 4*A*. (Detailed information about relaxivity and the T_1 relaxivity curves is shown in Fig. S6.) For the thinner shell (red), the r_1 relaxation was 24.5 $mM^{-1}{\cdot}s^{-1}$, whereas the thicker shell (yellow) yielded a significant decrease in r_1 relaxation, to 1.2 $mM^{-1}{\cdot}s^{-1}$. A dramatic reduction in T_1 contrast for the Gd-NM-PEG with the thicker outer layer was observed in T_1-weighted MR images (Fig. 4*B*). In the case of the thinner Au shell, small pinhole defects in the outer layer may be present that would slightly increase the H_2O proton interaction with the internal Gd(III), enhancing the r_1 relaxivity in this case. The corresponding TEM images of the Gd-NM-PEG nanoparticles with four different gold outer shell thicknesses are shown in Fig. 4*B*. (Detailed information about the extinction spectra of the Gd-NM-PEG nanoparticles with different gold outer shell thicknesses are shown in Figs. S7 and S8.) To analyze the observed MRI enhancement of the Gd-NM geometry, SBM theory (15, 36) was adopted to estimate the relaxivity r_1 of the Gd-NM:

$$r_1 = r_0 + r^{IS} + r^{OS}, \qquad [1]$$

where r_0 is the intrinsic relaxivity and r^{IS} and r^{OS} are inner-sphere and outer-sphere contributions to the total relaxivity, respectively. The intrinsic relaxivity and inner-sphere contributions are assumed to be negligible, because the Gd(III) chelates are embedded within the SiO_2 shell where few H_2O molecules are present relative to the NM surroundings. Also, it has been evidently shown in experiments that such intrinsic and inner-sphere contributions are very small. For instance, these contributions are not altered when varying the outer-shell Au thickness, but the r_1 drops to nearly zero (~1.2 $mM^{-1}{\cdot}s^{-1}$) when the outer-shell thickness is very large (~35 nm in Fig. 4). Therefore, we only focus on the outer-sphere contribution. According to SBM theory (15), the outer-sphere contribution is given by the following:

$$r^{OS} = \frac{C}{dD} Re[3j(\omega_I) + 7j(\omega_s)]. \qquad [2]$$

Here, C is a constant [for Gd(III) chelates, it is $C = 5.8 \times 10^{-19}$ $m^6{\cdot}s^{-2}{\cdot}mol^{-1}$] and d is the distance of closest approach of H_2O molecules. D is the sum of diffusion coefficients of bulk water and of the complex and is $D = 2.84 \times 10^{-9}$ $m^2{\cdot}s^{-1}$ (37), $j(\omega)$ is the spectral density function (15), with variable ω_I and ω_s, the proton and electronic Larmor angular frequencies, respectively. For our calculations, the parameters of Gd-DOTA were selected (15) in accordance with the experimental conditions and the magnetic field of 4.7 T. Considering the Gd(III) chelates are distributed within the silica layer, which is about 13 nm in average, and also the size variation of outer Au shell thickness is ±2 nm, we apply a twofold average for the r_1 calculations. First, the calculated r_1 values are averaged over a uniform distribution of Gd(III) locations inside the silica layer, leading to the averaged r_1 value for a certain outer Au shell thickness; second, we account for the size variation, and take three sizes in practice [d_{aver} − 2 nm, d_{aver}, d_{aver} + 2 nm], where d_{aver} stands for the averaged outer Au shell thickness. Then, we apply a weight-averaging procedure for the three different size cases, in which the weights are 25%, 50%, and 25%, respectively. Using such a twofold averaging calculation, we are able to calculate the relaxivity r_1 predicted by SBM theory, but the values are very small, only one-third of what we observed in experiments [the calculated longitudinal relaxivity r_1 of symmetric distribution of Gd(III) inside the silica layer vs. Au shell thickness with a concentration of 3×10^5 Gd(III) chelates per NM is presented in Fig. S9]. This is because there are additional factors not involved in our model. For instance, the Gd(III) distribution inside silica cannot be truly uniform, and some Gd(III) can even have shorter "closest distance" with outer water molecules compared with outer Au shell thickness. Thus, we need to modify the Gd(III) distribution in our model to match experimental data. In practice, the predicted SBM results are found to match experimental data well when more Gd(III) are

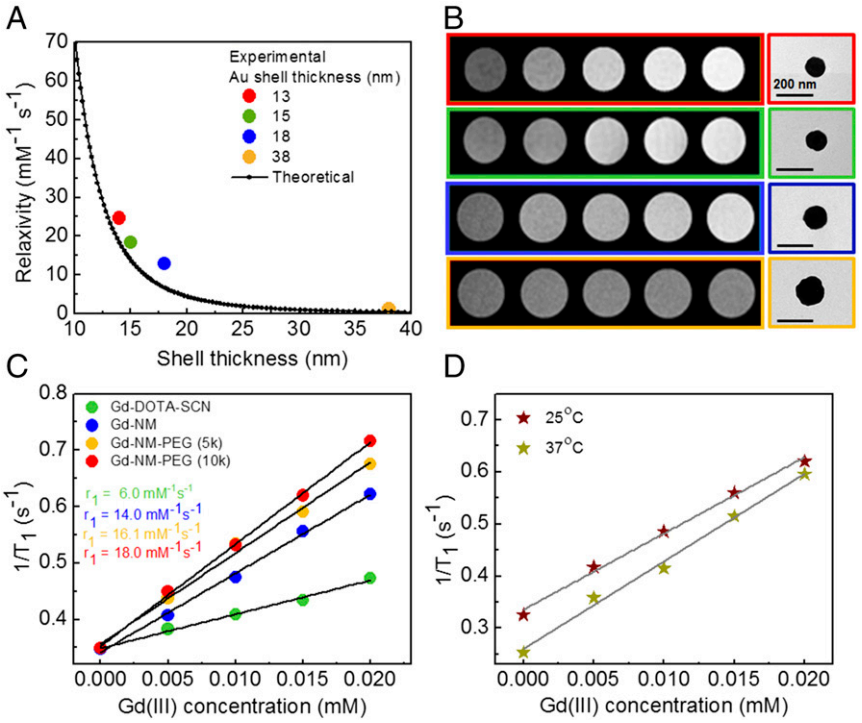

Fig. 4. (*A*) The calculated longitudinal relaxivity r_1 vs. Au shell thickness (solid line) using SBM theory [NM containing 2.3×10^5 Gd(III) chelates per particle], and the dots are the experimental data of Gd-NM-PEG (10,000) for four Au shell thicknesses of approximately (red) 13 nm, (green) 15 nm, (blue) 18 nm, and (orange) 38 nm; (*B*) the T_1-weighted MR images corresponding to the concentrations of 0, 5, 10, 15, and 20 μM Gd(III), and the TEM images. (Scale bar: 200 nm.) All measurements were performed at room temperature. (*C*) r_1 relaxivities of free Gd(III)-DOTA-SCN chelate, Gd-NM, and Gd-NM with 5,000 and 10,000 PEG; (*D*) Thermal variation of T_1 (longitudinal) rate of Gd(III)-NM-PEG at room temperature (~25 °C) (blue, $r_1 = 14.6$ mM^{-1}·s^{-1}) and at 37 °C (red, $r_1 = 16.1$ mM^{-1}·s^{-1}).

near the outer surface of silica layer, say 40% near the surface while the other 60% are uniformly distributed inside the silica layer as shown in Fig. 4*A*, where we use this analysis to plot the longitudinal relaxivity r_1 as a function of Au shell thickness for the Gd-NM nanoparticle geometry. The theoretical longitudinal relaxivity r_1 decreases with increasing Au shell thickness. The relaxivity for a Gd-NM with an 18-nm-thick Au shell was measured to be 12.9 mM^{-1}·s^{-1}, whereas the SBM theoretical value is just slightly smaller, ~8 mM^{-1}·s^{-1}; for the 38-nm shell, the relaxivity was measured to be 1.5 mM^{-1}·s^{-1}, whereas the theoretical value for this larger shell thickness is 0.5 mM^{-1}·s^{-1}. The results are in good agreement with the theoretical model (Fig. 4*A*). The larger value of the experimentally observed longitudinal relaxivity relative to the theoretical analysis may indicate an enhancement due to a combination of effects not included in the SBM model. Besides the large fraction of Gd(III) chelate located near the silica outer surface, as analyzed above, some other effects can also contribute to the enhancement of the relaxivity measured experimentally. For example, like other nanoparticles, the NMs can increase the correlation time of bulk water in their direct vicinity, 15 resulting in an r_1 enhancement. Also, Gd(III) is weakly ferromagnetic (38), as are Au nanoparticles under certain conditions (39). Therefore, the interplay between Gd(III) and Au spins can give rise to a small magnetization within the outer Au shell. Nearby H_2O molecules may experience additional magnetization at a reduced distance, leading to an enhanced r_1 relaxivity.

The nanoparticle relaxivity can also be affected by the stability of the nanoparticle. To prevent aggregation, the Gd-NMs were functionalized with thiolated PEG molecules of 5,000 M_r and 10,000 M_r (Fig. 4*C*). PEG functionalization improves NM dispersion in media and is known to increase circulation time in vivo (40). We observed that Gd-NM relaxivity increased with PEG functionalization, from 13.9 to 16.1 mM^{-1}·s^{-1} (5,000 M_r PEG) or 18 mM^{-1}·s^{-1} (10,000 M_r PEG) for an internal Gd(III) concentration of 2.5×10^5 Gd(III)/NM (Fig. 4*C*). We can infer from this increased relaxivity that the presence of PEG molecules on the surface of the nanoparticles facilitates the approach of water protons to the NM surface, closer to the internally encapsulated Gd(III) ions, and reduces the mobility of the nanocomplex. The diffusion of water in the proximity of the Gd(III) is known to play an important role in the enhancement of proton relaxivity (19, 29, 41–43). Besides Gd(III) concentration and surface functionalization, temperature can also affect the relaxivity, which can have a major impact in vivo (33). We compared the relaxivity measurements of Gd-NM-PEG at 37 °C and at room temperature (Fig. 4*D*). The relaxivities of Gd-NM-PEG were extracted from the slope of $1/T_1$ vs. Gd(III) concentration. The relaxivity was found to increase from $r_1 = 14.6$ mM^{-1}·s^{-1} when the ambient temperature of the nanoparticles was increased from room temperature to $r_1 = 16.1$ mM^{-1}·s^{-1} at physiological temperature. Although Gd-based liposomal structures also show increased relaxivities at physiological temperature, small–molecular-weight Gd-based contrast agents typically show reduced relaxivities with increasing temperature because the rotational correlation time is a limiting parameter for small molecules (44). Furthermore, to ensure that the MRI properties of the Gd-NM are not compromised due to laser exposure, the longitudinal relaxivity of Gd-NM was measured before and after the laser illumination (Fig. S10). The Gd-NM-PEG in PBS solutions (~10^9 particles per mL) was irradiated by a CW NIR (808-nm, 1-W) laser for 2 min followed by 5-min relaxation time. This cycle was repeated for a total of three cycles. Notably, the T_1 relaxation time did not change outside of the SD after each cycle. In addition, TEM images in Fig. S10 *B* and *C*

illustrate that the NM's morphology does not change under higher-power laser illumination and longer exposure time. A NIR CW laser source (808-nm wavelengths, 5-W power, 10-min illumination time) was used for this aqueous Gd-NM-PEG thermal stability study.

In summary, the Gd(III)-encapsulating NMs that we have designed and synthesized provide an excellent MRI T_1 enhancement while maintaining the NIR optical properties useful for photothermal applications. The sequestration of Gd(III) within the inner layer of the nanoparticle results in increased T_1 relaxivities relative to Gd(III)-based chelates currently in widespread use and is enhanced even further by PEG functionalization. The enhanced relaxivity is due to enhanced magnetization that water molecules experience because of the shorter effective closest distance, from the interplay between neighboring Gd(III) chelates and more Gd(III) located near silica surface. This phenomenon is well-described by our twofold averaging SBM calculations. Given the MRI contrast, photothermal properties, stability, and facile surface chemistry of gold for additional functionalization, Gd-NM-PEG have potential applications as multifunctional agents for both diagnosis and treatment. Increased cellular uptake of Gd(III) ions into specific tissues could be achieved by modifying the external Au shell of the Gd-NM with specific biological functional groups for targeting different types of cancer. Most importantly, the incorporation of Gd(III) into the NM structure may allow for tracking of particles in vivo and investigation of their biodistribution, which is essential to develop safer and more effective nanomaterials for medical applications.

Associated Content

SI Associated Content provides experimental details, including information on materials, Gd-NM synthesis, investigation of structural parameters on the relaxivity of the Gd-NM, Au-shell thickness, FTIR spectra of the NMs at various synthesis steps, TEM images, and optical spectra of the NMs.

ACKNOWLEDGMENTS. We thank Budi Utama and Ben Cerjan for helping with measurements, and Amanda Goodman and Alejandra Garcia Piantanida for discussions. We also acknowledge the Sao Paulo Research Foundation (FAPESP) Grant 2014/13645-2 for the doctorate research internships abroad (Bolsa Estágio de Pesquisa no Exterior-DR). We also acknowledge the J. Evans Attwell–Welch Fellowship (L-C-0004), the Welch Foundation (C-1220 and C-1222), and the NIH (U01 CA 151886 and 5R01 CA 151962).

1. Shevchenko EV, et al. (2008) Gold/iron oxide core/hollow-shell nanoparticles. *Adv Mater* 20:4323–4329.
2. Kim T, et al. (2011) Mesoporous silica-coated hollow manganese oxide nanoparticles as positive T1 contrast agents for labeling and MRI tracking of adipose-derived mesenchymal stem cells. *J Am Chem Soc* 133:2955–2961.
3. Gao J, et al. (2008) Multifunctional yolk-shell nanoparticles: A potential MRI contrast and anticancer agent. *J Am Chem Soc* 130:11828–11833.
4. Narayanan S, et al. (2012) Biocompatible magnetite/gold nanohybrid contrast agents via green chemistry for MRI and CT bioimaging. *ACS Appl Mater Interfaces* 4:251–260.
5. O'Neal DP, Hirsch LR, Halas NJ, Payne JD, West JL (2004) Photo-thermal tumor ablation in mice using near infrared-absorbing nanoparticles. *Cancer Lett* 209:171–176.
6. Bardhan R, Lal S, Joshi A, Halas NJ (2011) Theranostic nanoshells: From probe design to imaging and treatment of cancer. *Acc Chem Res* 44:936–946.
7. Lim E-K, et al. (2015) Nanomaterials for theranostics: Recent advances and future challenges. *Chem Rev* 115:327–394.
8. Yong K-T, Roy I, Swihart MT, Prasad PN (2009) Multifunctional nanoparticles as biocompatible targeted probes for human cancer diagnosis and therapy. *J Mater Chem* 19:4655–4672.
9. Merbach AS, Helm L, Toth E (2013) *The Chemistry of Contrast Agents in Medical Magnetic Resonance Imaging* (Wiley, New York).
10. Agulla J, et al. (2014) Quick adjustment of imaging tracer payload, for in vivo applications of theranostic nanostructures in the brain. *Nanomedicine (Lond)* 10: 851–858.
11. Naa HB, Hyeon T (2009) Nanostructured T_1 MRI contrast agents. *J Mater Chem* 19: 6267–6273.
12. Na HB, Song IC, Hyeon T (2009) Inorganic nanoparticles for MRI contrast agents. *Adv Mater* 21:2133–2148.
13. Dumas S, et al. (2010) High relaxivity magnetic resonance imaging contrast agents. Part 1. Impact of single donor atom substitution on relaxivity of serum albumin-bound gadolinium complexes. *Invest Radiol* 45:600–612.
14. Yang JJ, et al. (2008) Rational design of protein-based MRI contrast agents. *J Am Chem Soc* 130:9260–9267.
15. Ananta JS, et al. (2010) Geometrical confinement of gadolinium-based contrast agents in nanoporous particles enhances T_1 contrast. *Nat Nanotechnol* 5:815–821.
16. Wen S, et al. (2013) Multifunctional dendrimer-entrapped gold nanoparticles for dual mode CT/MR imaging applications. *Biomaterials* 34:1570–1580.
17. Liu Y, et al. (2011) Gadolinium-loaded polymeric nanoparticles modified with anti-VEGF as multifunctional MRI contrast agents for the diagnosis of liver cancer. *Biomaterials* 32:5167–5176.
18. Coughlin AJ, et al. (2014) Gadolinium-conjugated gold nanoshells for multimodal diagnostic imaging and photothermal cancer therapy. *Small* 10:556–565.
19. Rotz MW, et al. (2015) High relaxivity Gd(III)-DNA gold nanostars: Investigation of shape effects on proton relaxation. *ACS Nano* 9:3385–3396.
20. Ayala-Orozco C, et al. (2014) Au nanomatryoshkas as efficient near-infrared photothermal transducers for cancer treatment: Benchmarking against nanoshells. *ACS Nano* 8:6372–6381.
21. Ayala-Orozco C, et al. (2014) Sub-100 nm gold nanomatryoshkas improve photothermal therapy efficacy in large and highly aggressive triple negative breast tumors. *J Control Release* 191:90–97.
22. Jain S, Hirst DG, O'Sullivan JM (2012) Gold nanoparticles as novel agents for cancer therapy. *Br J Radiol* 85:101–113.
23. Ayala-Orozco C, et al. (2014) Fluorescence enhancement of molecules inside a gold nanomatryoshka. *Nano Lett* 14:2926–2933.
24. Sinigaglia G, et al. (2012) Catalytically active bovine serum amine oxidase bound to fluorescent and magnetically drivable nanoparticles. *Int J Nanomedicine* 7:2249–2259.
25. Xu S, Hartvickson S, Zhao JX (2011) Increasing surface area of silica nanoparticles with a rough surface. *ACS Appl Mater Interfaces* 3:1865–1872.
26. Ding T, Yao L, Liu C (2016) Kinetically-controlled synthesis of ultra-small silica nanoparticles and ultra-thin coatings. *Nanoscale* 8:4623–4627.
27. Liberman A, Mendez N, Trogler WC, Kummel AC (2014) Synthesis and surface functionalization of silica nanoparticles for nanomedicine. *Surf Sci Rep* 69:132–158.
28. Barisik M, Atalay S, Beskok A, Qian S (2014) Size dependent surface charge properties of silica nanoparticles. *J Phys Chem C* 118:1836–1842.
29. Tóth É, Pubanz D, Vauthey S, Helm L, Merbach AE (1996) The role of water exchange in attaining maximum relaxivities for dendrimeric MRI contrast agents. *Chemistry* 2: 1607–1615.
30. Rohrer M, Bauer H, Mintorovitch J, Requardt M, Weinmann HJ (2005) Comparison of magnetic properties of MRI contrast media solutions at different magnetic field strengths. *Invest Radiol* 40:715–724.
31. Kielar F, Tei L, Terreno E, Botta M (2010) Large relaxivity enhancement of paramagnetic lipid nanoparticles by restricting the local motions of the Gd(III) chelates. *J Am Chem Soc* 132:7836–7837.
32. Bruckman MA, Yu X, Steinmetz NF (2013) Engineering Gd-loaded nanoparticles to enhance MRI sensitivity via T_1 shortening. *Nanotechnology* 24:462001–462037.
33. Caravan P, Farrar CT, Frullano L, Uppal R (2009) Influence of molecular parameters and increasing magnetic field strength on relaxivity of gadolinium- and manganese-based T_1 contrast agents. *Contrast Media Mol Imaging* 4:89–100.
34. Maeda H, Bharate GY, Daruwalla J (2009) Polymeric drugs for efficient tumor-targeted drug delivery based on EPR-effect. *Eur J Pharm Biopharm* 71:409–419.
35. Merbach A, Helm L, Tóth E (2013) *The Chemistry of Contrast Agents in Medical Magnetic Resonance Imaging* (Wiley, Chichester, UK), 2nd Ed.
36. Lauffer RB (1987) Paramagnetic metal complexes as water proton relaxation agents for NMR imaging: Theory and design. *Chem Rev* 87:901–927.
37. Vander Elst L, Sessoye A, Laurent S, Muller RN (2005) Can the theoretical fitting of the proton-nuclear-magnetic-relaxation-dispersion (proton NMRD) curves of paramagnetic complexes be improved by independent measurement of their self-diffusion coefficients? *Helv Chim Acta* 88:574–587.
38. Svitova AL, et al. (2014) Magnetic moments and exchange coupling in nitride clusterfullerenes $Gd_xSc_{3-x}N@C_{80}$ (x = 1–3). *Dalton Trans* 43:7387–7390.
39. Nealon GL, et al. (2012) Magnetism in gold nanoparticles. *Nanoscale* 4:5244–5258.
40. Jokerst JV, Lobovkina T, Zare RN, Gambhir SS (2011) Nanoparticle PEGylation for imaging and therapy. *Nanomedicine (Lond)* 6:715–728.
41. Strauch RC, et al. (2011) Reporter protein-targeted probes for magnetic resonance imaging. *J Am Chem Soc* 133:16346–16349.
42. Cho M, et al. (2014) Gadolinium oxide nanoplates with high longitudinal relaxivity for magnetic resonance imaging. *Nanoscale* 6:13637–13645.
43. Sun G, Feng J, Jing F, Pei F, Liu M (2003) Synthesis and evaluation of novel polysaccharide-Gd-DTPA compounds as contrast agent for MRI. *J Magn Magn Mater* 265:123–129.
44. Raymond KN, Pierre VC (2005) Next generation, high relaxivity gadolinium MRI agents. *Bioconjug Chem* 16:3–8.
45. Duff DG, Baiker A, Edwards PP (1993) A new hydrosol of gold clusters. 1. Formation and particle size variation. *Langmuir* 9:2301–2309.
46. Bardhan R, et al. (2010) Nanosphere-in-a-nanoshell: A simple nanomatryushka. *J Phys Chem C* 114:7378–7383.
47. Sohaebuddin SK, Thevenot PT, Baker D, Eaton JW, Tang L (2010) Nanomaterial cytotoxicity is composition, size, and cell type dependent. *Part Fibre Toxicol* 7:22.
48. Johnson PB, Christy RW (1972) Optical constants of the noble metals. *Phys Rev B* 6:4370–4379.

Supporting Information

Marangoni et al. 10.1073/pnas.1701944114

SI Associated Content

Materials. Tetraethoxysilane (TEOS) and 3-aminopropyl)triethoxysilane (APTES) were purchased from Gelest; *S*-2 (4-isothiocyanatobenzyl)-1,4,7,10-tetraazacyclododecane-1,4,7,10-tetraacetic acid (Gd-DOTA-SCN) was purchased from Macrocyclics; tetrakis(hydroxymethyl) phosphonium chloride (THPC), $Gd(NO_3)_3 0.6H_2O$, and chloroauric acid ($HAuCl_4 0.3H_2O$) were purchased from Sigma-Aldrich; anhydrous potassium carbonate (K_2CO_3) was from Fisher; mPEG-Thiol (M_r = 10,000) was from Laysan Bio; and NaOH was from Fisher and used without further purification. The 50-nm gold colloid citrate NanoXact was purchased from NanoComposix. DMEM was purchased from ATCC; FBS, PBS, and antibiotic–antimycotic solution were from CellGro; and RAW 264.7 macrophage cells were purchased from Sigma-Aldrich. The 200-proof ethanol was purchased from KOPTEC. SYTOX Red dead cell stain was purchased from Invitrogen. Aqua regia was used to clean all glassware and stir bars, followed by thorough rinsing with distilled water, ethanol, and Milli-Q water in the last step. Milli-Q water (18.2 MΩ·cm at 25 °C; Millipore) was used to prepare all solutions and reagents without further purification.

Gd-Embedded Au Nanomatryoshkas Synthesis. The synthesis of Gd-embedded Au nanomatryoshkas (Gd-NMs) developed in this study was adapted from the previously reported synthesis of fluorescent dye encapsulated NM by Ayala-Orozco et al. (21, 23). The 50-nm Au nanoparticles were initially coated with an amorphous SiO_2 layer by the condensation of tetraethyl orthosilicate in an alkaline medium. Briefly, 21 mL of 50-nm Au colloid solution (0.05 mg/mL) was mixed with 180 mL of 200-proof fresh ethanol under magnetic stirring, and subsequently, 1.8 mL of ammonium hydroxide were quickly added followed by 36 μL of 10% TEOS solution in ethanol and 21 μL of 10% APTES solution in ethanol. The reaction vessel was sealed and allowed to proceed for 75 min at room temperature under vigorous stirring and then stored in the refrigerator under gentle stirring at 4 °C. After 165 min (total reaction time), a mixture previously prepared containing a SCN-DOTA chelate was added. The mixture contains the following: 15 μL of Milli-Q H_2O, 5.5 mg of SCN-DOTA, 125 μL of ethanol, and 8 μL of a 20% APTES ethanolic solution. This mixture was kept at least 1 h under gentle stirring at room temperature and protected from light. After the addition of the chelate mixture to the nanoparticle suspension, the system was maintained under gentle stirring at 4 °C for a total reaction time of 27 h. The Gd(III) ions were incorporated into the APTES-doped silica layer of the NM by using a covalent strategy. More specifically, the SCN groups of the DOTA chelate *S*-2(4-isothiocyanatobenzyl)-1,4,7,10-tetraazacyclododecane-1,4,7,10-tetraacetic acid was bound to the amine groups of the APTES.

The following day, the Au/SiO_2 nanoparticles were transferred into a prewashed (200-proof ethanol) dialysis membrane (Spectra/Por 6; MWCO = 10,000; Spectrum Labs) and dialyzed in 1 gallon of 200-proof ethanol for 16 h at room temperature to remove the remaining free reagents. The cleaned nanoparticle suspension was cooled to 4 °C for at least 2 h and centrifuged for 35 min at 1,700 × *g*. The supernatant was removed and the pellets were dispersed in 3 mL of 11 mg/mL $Gd(NO_3)_3$ aqueous fresh solution to load the Gd(III) ions into the chelates. The system was then sonicated for 10 min, kept at room temperature for 100 min, and sonicated again for 10 min. The suspension was centrifuged at 1,800 × *g* for 25 min, and the pellet was dispersed in 2 mL of water, and then centrifuged one more time at 1,500 × *g* for 25 min. The cleaned pellet was dispersed in 1 mL of water and sonicated for 5 min. $Gd(NO_3)_3$ was added to load the Gd(III) ions onto the chelate. The $Au/SiO_2/Au$ nanoparticles were prepared by decorating the silica-coated nanoparticles with small gold colloid (2–3 nm) fabricated by the method reported by Duff et al. (45). Briefly, 1 mL of the Gd(III)-doped silica-coated gold nanoparticle suspension was mixed with 600 μL of 1 M NaCl and 40 mL of Duff gold colloid (1–2 nm). The precursor particles were left unperturbed for 24 h at room temperature, followed by sonication and centrifugation (950 × *g*, 30 min) to remove the excess of Duff gold colloid. The pellet was dispersed in 2 mL of Milli-Q water and centrifuged two more times at 800 × *g* for 20 min. The final precipitate was dispersed in 500 μL of Milli-Q H_2O and is called the seeded precursor. The formation of a continuous metallic shell around the seeded precursor was performed by mixing 3 mL of plating solution (1% $HAuCl_4$-K_2CO_3 solution previously prepared) with 20–40 μL of the seeded precursor and 15 μL of formaldehyde, under a fast shaking for 1 min. The color of the solution changed from reddish to purple upon the formation of the gold outer shell. The concentration of Gd(III) in the NMs were determined by inductively coupled plasma mass spectroscopy (ICP-MS). The measurements were performed in a Perkin-Elmer Nexion 300. First, the Gd-NM samples were dispersed in concentrated aqua regia (HNO_3:HCl, 1:3) solution overnight. The resulting solution was diluted by 500 times with a solution consisting of 1% (vol/vol) aqua regia, and 2% (vol/vol) HNO_3 solution was used for ICP-MS analysis. The Gd(III) concentration was determined using a calibration curve made with gadolinium ICP/DCP standard solution (Fluka).

Investigation of Structural Parameters on the r_1 Relaxivity of the Gd-NM. Influence of the number of Gd(III) ions per particle. The number of Gd(III) ions per particle was varied by adding different amounts of SCN-DOTA (from 4.0 to 7 mg) and consequently the amount of APTES ethanolic solution to maintain the same proportion in the mixture. The total reaction time was also varied between 24 and 27 h to ensure the same silica thickness. All other conditions and concentrations were kept the same as described previously.

Gold Shell Thickness. The seeded precursor was prepared as described in *Gd-Embedded Au Nanomatryoshkas Synthesis*. The seeded precursor suspension was divided in four groups. For each one, different amounts of seed were added to the plating solution (1% $HAuCl_4$-K_2CO_3 solution previously prepared) and formaldehyde, under a fast shaking for 1 min. Using less seeded precursor led to a thicker gold layer. The thickness was monitored experimentally by UV-VIS-NIR spectroscopy, that is, by increasing the gold layer, the second band peak of the NM structure blue shifts (Fig. S5). The thicknesses of the gold layer in each of the four systems were measured by TEM images using the digital micrograph program. The final Gd(III) concentration was determined by ICP-MS, and the suspensions were diluted to 5, 10, 15, and 20 μM [based on Gd(III) concentration] for the MRI measurements.

Surface Functionalization with PEG. Gd-NM was prepared as described in *Gd-Embedded Au Nanomatryoshkas Synthesis*. The resultant particle suspension was then divided into three groups. One was kept without further functionalization. The other two

were functionalized with thiolated mPEG. For this, 3 mL of $\sim 3 \times 10^{10}$ particles per mL aqueous nanoparticles were mixed with a freshly prepared mPEG-Thiol (M_r = 5,000; Laysan Bio) or mPEG-Thiol (M_r = 10,000; Laysan Bio) aqueous solution under sonication to a final solution concentration of 100 μmol/L. The system was sonicated for 30 min and then kept under gentle stirring and protected from light for 12 h. The systems were centrifuged at 700 × *g* for 20 min and resuspended in 500 μL of Milli-Q water. To avoid any influence of the additional centrifugation process, the nonfunctionalized system was also centrifuged at the same conditions. The final Gd(III) concentration of each system was determined by ICP-MS, and the suspensions were diluted to 5, 10, 15, and 20 μM [based on Gd(III) concentration] for the MRI measurements (Fig. S4).

Instrumentation. TEM using a JEOL 1230 operating at 80 kV and JEOL 2010 TEM operating at 200 kV was used. Fourier transform infrared (FTIR) spectroscopy of a DOTA-SCN solution, Au@SiO_2-SCN-DOTA, and Au@SiO_2-SCN-DOTA deposited on silicon substrates were obtained with a resolution of 4 cm^{-1} in absorbance mode using a Vertex 80v FTIR Spectrometer (Bruker). Cary 5000 UV/Vis/NIR Varian spectrophotometer was used to measure the extinction spectra of the nanoparticles. The ζ-potential of the nanostructures in suspension in each step of the synthesis process was performed by using a Malvern Nano-ZS spectrometer (Malvern Instruments). Inductively coupled plasma mass spectrometer (Perkin-Elmer; Nexion 300 ICP-MS) was used to determine the concentration of gadolinium ions after each synthesis. Briefly, the Gd-NM samples were mixed with concentrated aqua regia (HNO_3:HCl, 1:3) solution overnight. The resulting solution was diluted by 500 times with a solution consisting of 1% (vol/vol) aqua regia, and 2% (vol/vol) HNO_3 solution used for ICP-MS analysis. The concentration was determined using a calibration curve made with gadolinium ICP/DCP standard solution (Fluka).

MRI. All relaxation measurements were performed on a 4.7-T Biospec system (Bruker Biospin MRI) with a 30-cm bore, using imaging gradients with an inner diameter of 60 mm and a volume resonator with 35-mm inner diameter. Dilutions of the particle solution were sealed in 200-μL PCR tubes and placed in a holder. Spin-lattice (T_1) relaxation times were measured using a RARE variable repetition time (TR) sequence [echo time (TE) = 10.5 ms; with 10 TRs from 15,000 to 400 ms]. Spin-spin (T_2) relaxation times were measured using a multiecho sequence (TEmin = 10 ms, with 10-ms echo spacing over 30 echoes; TR = 5,000 ms). All images were acquired with matching slice geometry (1-mm axial sections, 32 mm × 32 mm field-of-view over a 256 × 256 image matrix). Relaxation time constants for each sample were measured by fitting signal decay curves to a standard model in ParaVision 5, the operating software for the Biospec platform.

To investigate the effect of water molecules accumulation in the silica inner layer, the Gd-NMs were synthetized as described in the manuscript, washed by centrifugation twice, and resuspended in D_2O. The weight T1 MR images of Gd-NM in D_2O images are presented in Fig. S4.

The relaxivity of Gd-NM with 2.8×10^5 Gd^{3+} ions per particle at 1 T was 54 $mM^{-1} \cdot s^{-1}$.

The final Au shell of Gd-NM was ∼10 ± 1 nm. As can be seen in Fig. S5, the suspension of the Gd-NM in D_2O leads to suppression of the MRI signal; this result may be an indication that the amount of water inside the silica shell is not enough to produce a significant MRI signal.

Tunability of Gd-NM. The extinction spectra of the Gd-NM-PEG nanoparticles with different gold outer-shell thicknesses are shown in Fig. S7. Experimentally, the shifts in the extinction spectra from 747 to 705 nm and 550 to 560 nm (Fig. S7 *A–D*) correspond to the reduced interlayer plasmon coupling resulting from increasing the thickness of the outer Au shell layer (46, 47). Using the finite-element method (FEM) (COMSOL software), we can model the pure NM system and calculate the extinction spectra as a function of incident light [Johnson and Christy (48) data for Au permittivity, water medium]. The sizes of outer-shell Au thickness are chosen to be ∼13, 15, 18, and 38 nm (Fig. S7 *I–L*) to match the peak positions of observed extinction spectra in experiments. The amplitudes of the two plasmonic modes in simulations are different compared with experiments, which may be attributed to the mismatch of real size, shape, and symmetry of the synthetized NM. In particular, a large amount of Gd(III) chelates is embedded in the inner silica layer, which will certainly change the dielectric function of silica, and thus alter the line-shape of the extinction spectra. However, we used the permittivity of pure silica (refractive index n = 1.5) in calculations (Fig. S7 *I–L*); a good approximate value for the true dielectric constant of silica is in experiments. Furthermore, the corresponding field enhancement maps of the lower-energy plasmonic mode are shown in Fig. S7 *E–H*, indicating a clearly weaker plasmon coupling strength with increasing outer-shell Au thickness.

As seen in Fig. S9, the r_1 decreases very fast (nearly exponentially) with increasing outer-shell length. The Gd(III) near the outermost of the silica provides the greatest contribution to the relaxivity. That is why we use the outer-shell length as the "closest distance" between Gd and water molecule. Fig. S9 presents the predicted relativity with Gd(III) uniformly distributed within silica (blue line), of GdNM with [r1′,r2′] = [25 nm, 38 nm]. Here, we can see that the predicted relaxivity significantly decreases due to longer interaction distances, and the measured relaxivities (dots) are much larger than predicted values. These differences arise from the contribution of Gd(III) residing near the interface between silica and outer Au shell.

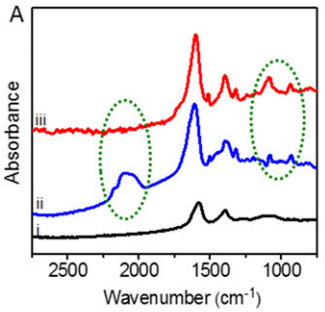

Au@SiO_2APTES	Gd-DOTA-SCN	Au@SiO_2-APTS-Gd-DOTA-SCN	Peak assignments
1580	---	1607	NH_2 (def)
1390	---	1396	C-N (str)
1089	---	1084	Si-O-Si (str)
---	2100	---	N=C=S (str)
---	1626	1607	COO^- (str)
---	1396	1396	COO^- (str)

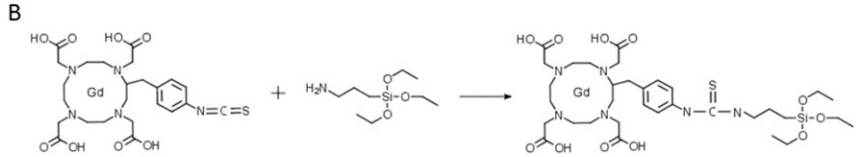

Fig. S1. (*A*) FTIR spectra of (*i*) Au@SiO_2-APTES, (*ii*) SCN-DOTA, and (*iii*) SCN-DOTA-modified–SiO_2-coated Au colloid. The disappearance of the 2,100 cm^{-1} peak, attributed to the N=C=S vibration, is an indication of the bond between SCN-DOTA and the amine groups from APTES. (*B*) The chemical reaction showing the bond formation. The table shows the FTIR peak assessments corresponding to each spectrum.

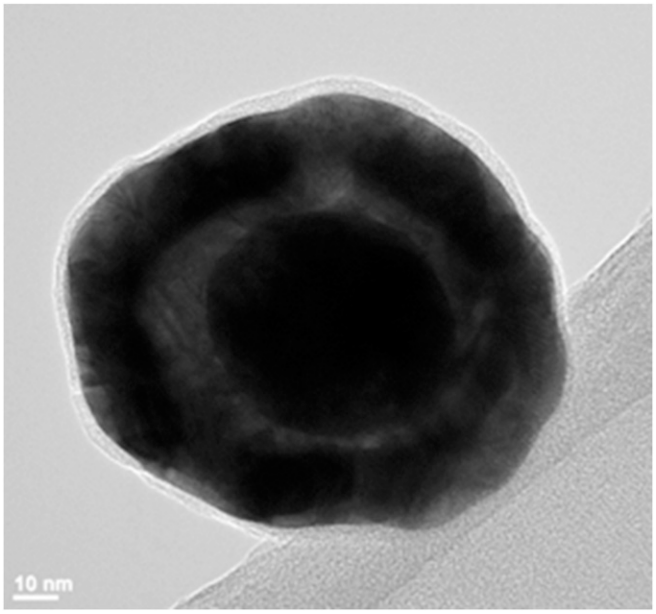

Fig. S2. High-resolution TEM of Gd-NM-PEG showing the complete gold outer shell and the PEG layer.

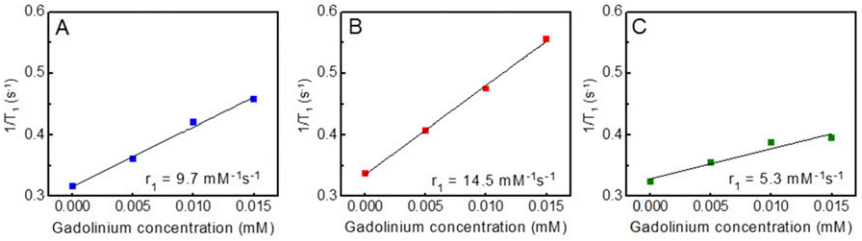

Fig. S3. T_1 (longitudinal) rate of Gd-NM for (*A*) 0.8×10^5, (*B*) 2.7×10^5, and (*C*) 8.2×10^5 numbers of Gd^{3+} ions per particle at 4.7 T. The r_1 values were extracted from the slopes.

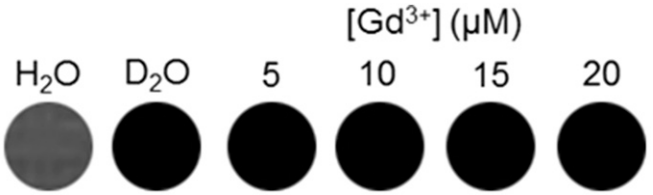

Fig. S4. Weight T_1 MR images of Gd-NM suspended in D_2O; corresponding to the concentrations of 0, 5, 10, 15, and 20 μM Gd(III) at 4.7 T.

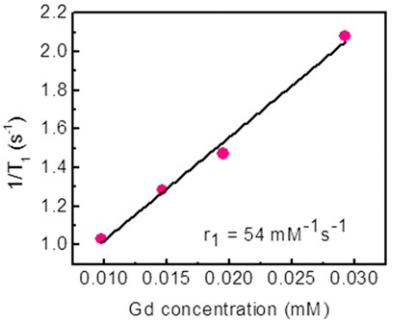

Fig. S5. T_1 (longitudinal) rate of Gd-NM of 2.8 x 10^5 numbers of Gd^{3+} ions per particle at 1 T. The r_1 values were extracted from the slopes.

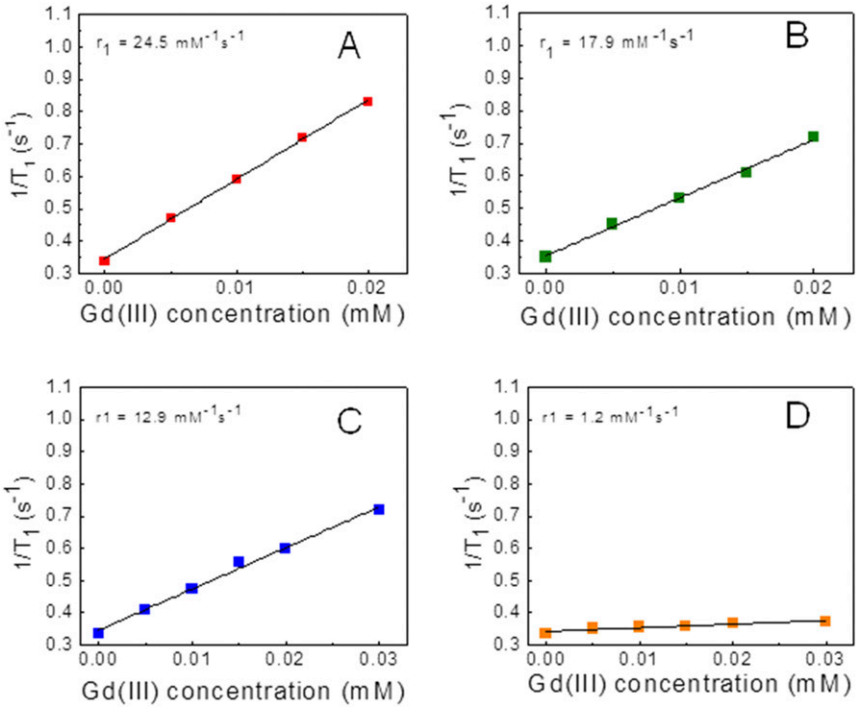

Fig. S6. Longitudinal T_1 rate vs. Gd(III) concentration at 4.7 T of Gd-NM-PEG for four Au shell thicknesses of approximately (*A*) 13 nm, (*B*) 15 nm, (*C*) 18 nm, and (*D*) 38 nm. In all cases, the concentration of Gd(III) ions per NM was 2.3×10^5.

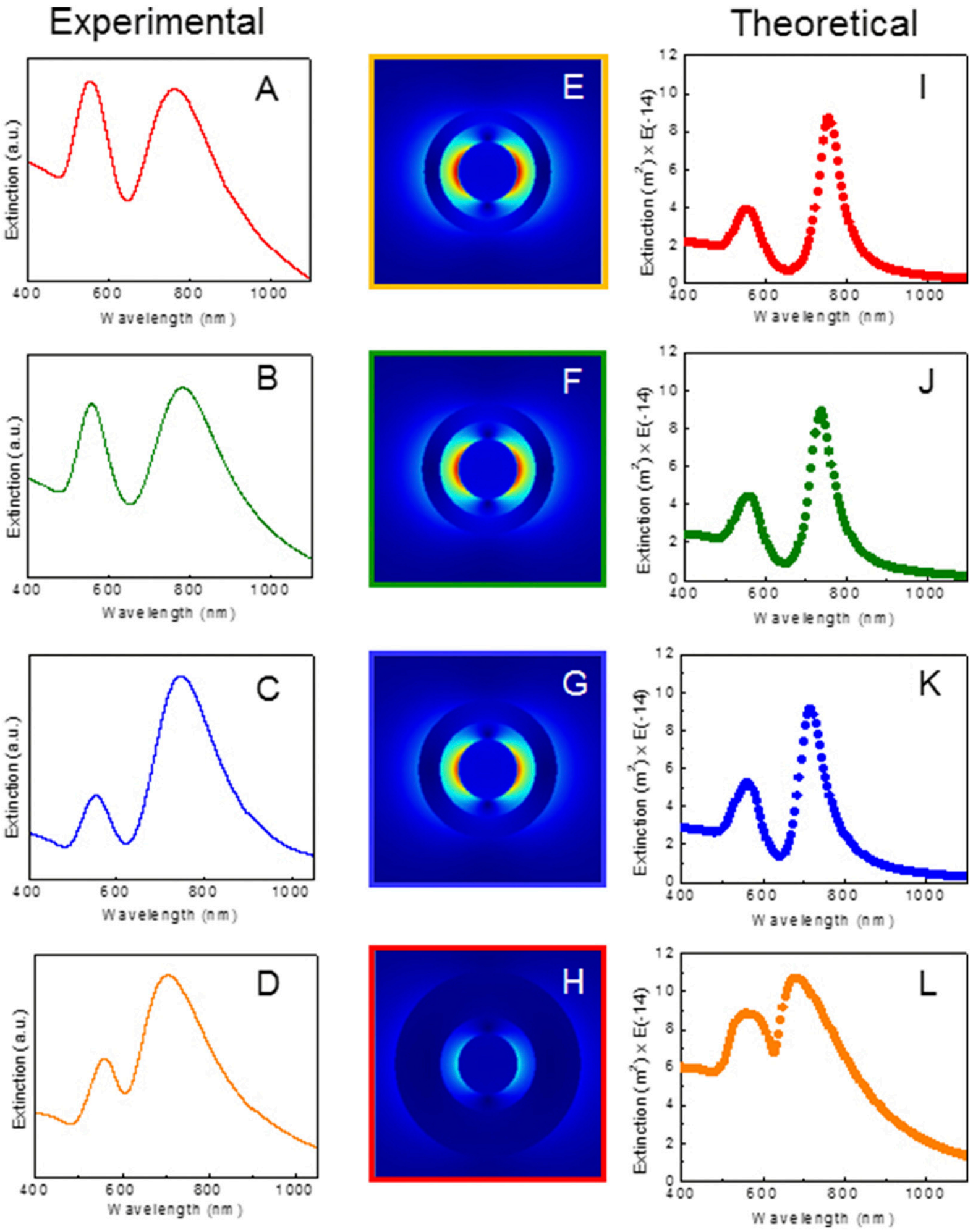

Fig. S7. Extinction spectra of Gd-NM-PEG for four Au shell thicknesses of approximately (*A*) 13 nm, (*B*) 15 nm, (*C*) 18 nm, (*D*) 38 nm, and the corresponding (*E*–*H*) field enhancement at the low-energy peak position, and (*I*–*L*) theoretical extinction spectra under water medium using the finite-element method (FEM) (COMSOL software). In all cases, the concentration of Gd(III) ions per NM was 2.3×10^5.

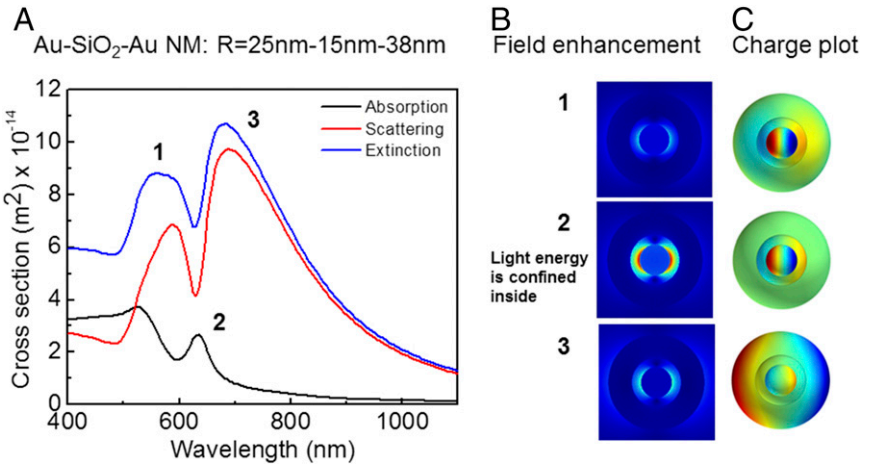

Fig. S8. Theoretical simulations for the 25-nm–15-nm–38-nm Au–SiO_2–Au NM (FEM method; COMSOL software) indicating a clear Fano effect. (*A*) Cross-sections of absorption, scattering, and extinction with varying the light wavelength, where 1, 3 denote the peak positions of extinction spectra, and 2 denotes the peak position of absorption spectra (also the dip position of scattering spectra). (*B*) Corresponding field enhancements at different positions. (*C*) Corresponding charge distribution plot at these peak positions, showing the distinct plasmon modes.

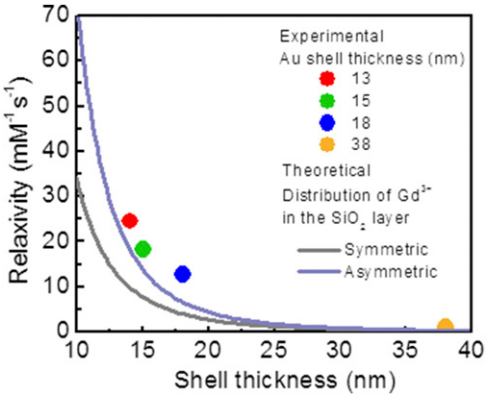

Fig. S9. The calculated longitudinal relaxivity r_1 of (blue) asymmetric and (gray) symmetric distribution of Gd(III) inside the silica layer vs. Au shell thickness using the SBM theory (solid line) [a concentration of 3×10^5 Gd(III) chelates per NM is used], and the dots are the experimental data of Gd-NM-PEG for four Au shell thicknesses of approximately (red) 13 nm, (green) 15 nm, (blue) 18 nm, and (orange) 38 nm.

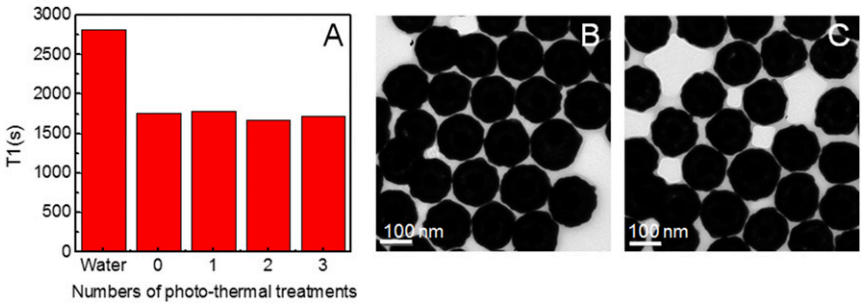

Fig. S10. (*A*) T_1 longitudinal rate of Gd-NM at 4.7 T vs. number of photothermal illumination cycles. Each Gd-NM PBS solution was illuminated with 1 W of CW (808-nm) laser for 2 min. TEM images of Gd-NM (*B*) before and (*C*) after laser treatment, showing that the NM's morphology does not change under the laser illumination.